Accepted Manuscript

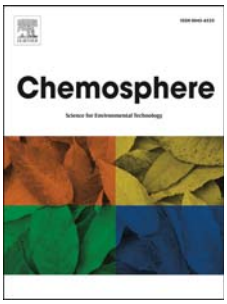

Removal of lead from aqueous solution using superparamagnetic palygorskite nanocomposite: Material characterization and regeneration studies

Ruhaida Rusmin, Binoy Sarkar, Takuya Tsuzuki, Nobuyuki Kawashima, Ravi Naidu

PII: S0045-6535(17)31259-6

DOI: 10.1016/j.chemosphere.2017.08.036

Reference: CHEM 19734

To appear in: *ECSN*

Received Date: 21 February 2017

Revised Date: 28 July 2017

Accepted Date: 9 August 2017

Please cite this article as: Rusmin, R., Sarkar, B., Tsuzuki, T., Kawashima, N., Naidu, R., Removal of lead from aqueous solution using superparamagnetic palygorskite nanocomposite: Material characterization and regeneration studies, *Chemosphere* (2017), doi: 10.1016/j.chemosphere.2017.08.036.

Graphical abstract

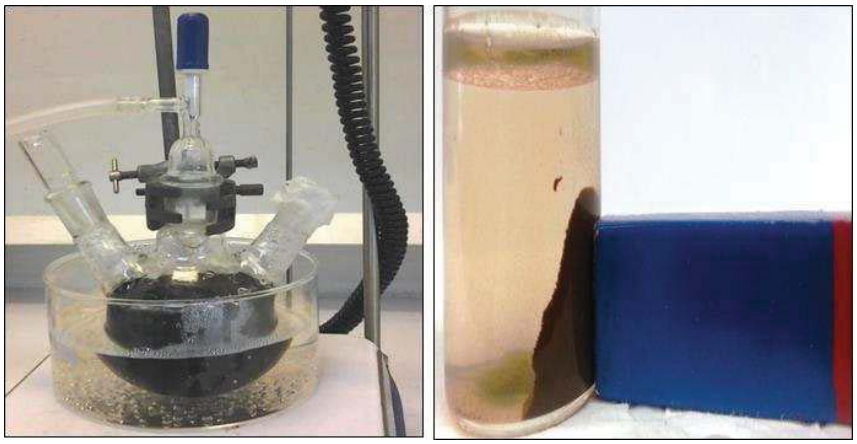

Removal of lead from aqueous solution using superparamagnetic palygorskite nanocomposite: material characterization and regeneration studies

Ruhaida Rusmin[a,b*], *Binoy Sarkar*[a§*], *Takuya Tsuzuki*[c], *Nobuyuki Kawashima*[a], *Ravi Naidu*[d,e*]

[a] Future Industries Institute, University of South Australia, Building X, Mawson Lakes, SA 5095, Australia.

[b] Faculty of Applied Sciences, Universiti Teknologi MARA, 40450, Shah Alam, Selangor, Malaysia.

[c] Research School of Engineering, College of Engineering and Computer Science, Australian National University, Acton, ACT 2601, Australia.

[d] Global Centre for Environmental Remediation (GCER), The University of Newcastle, ATC Building, Callaghan, NSW 2308, Australia.

[e] CRC CARE – Cooperative Research Centre for Contamination Assessment and Remediation of the Environment, P.O. Box 486, Salisbury, SA 5106, Australia.

[§] Current address: Department of Animal and Plant Sciences, The University of Sheffield, Western Bank, Sheffield, S10 2TN, UK.

[*]Corresponding authors:

E-mail: Binoy.Sarkar@unisa.edu.au (Binoy Sarkar)

E-mail: Ravi.Naidu@newcastle.edu.au (Ravi Naidu)

E-mail: ruhaida.rusmin@mymail.unisa.edu.au (Ruhaida Rusmin)

Abstract

A palygorskite-iron oxide nanocomposite (Pal-IO) was synthesized *in situ* by embedding magnetite into the palygorskite structure through co-precipitation method. The physico-chemical characteristics of Pal-IO and their pristine components were examined through various spectroscopic and micro-analytical techniques. Batch adsorption experiments were conducted to evaluate the performance of Pal-IO in removing Pb(II) from aqueous solution. The surface morphology, magnetic recyclability and adsorption efficiency of regenerated Pal-IO using desorbing agents HCl (Pal-IO-HCl) and ethylenediaminetetraacetic acid disodium salt (EDTA-Na_2) (Pal-IO-EDTA) were compared. The nanocomposite showed a superparamagnetic property (magnetic susceptibility: 20.2 emu g^{-1}) with higher specific surface area (99.8 m^2 g^{-1}) than the pristine palygorskite (49.4 m^2 g^{-1}) and iron oxide (72.6 m^2 g^{-1}). Pal-IO showed a maximum Pb(II) adsorption capacity of 26.6 mg g^{-1} (experimental condition: 5 g L^{-1} adsorbent loading, 150 agitations min^{-1}, initial Pb(II) concentration from 10 to 500 mg L^{-1}, at 25°C) with easy separation of the spent adsorbent. The adsorption data best fitted to the Langmuir isotherm model (R^2=0.9995) and pseudo-second order kinetic model (R^2=0.9945). Pb(II) desorption using EDTA as the complexing agent produced no disaggregation of Pal-IO crystal bundles. and was able to preserve the composite's magnetic recyclability. Pal-IO-EDTA exhibited almost 64% removal capacity after three cycles of regeneration and preserved the nanocomposite's structural integrity and magnetic properties (15.6 emu g^{-1}). The nanocomposite holds advantages as a sustainable material (easily separable and recyclable) for potential application in purifying heavy metal contaminated wastewaters.

Key words: Palygorskite-iron oxide nanocomposite; Magnetic separation; Lead contamination; Desorption; Regeneration

1. Introduction

The heavy metal lead (Pb) ranks second in the Substance Priority List compiled by the Agency for Toxic Substances and Disease Registry (ATSDR) (ATSDR, 2015), which indicates the serious health and the environmental risk of this metal. Anthropogenically Pb(II) can occur in water sources through leaching and improper discharge from aging plumbing infrastructure, smelting activities, e-waste recycling and mining industries (Harvey et al., 2015; Yoshida et al., 2016). The Pb(II) contamination of water and soil remains a challenge primarily for less-developed countries due to the ineffective infrastructure, less stringent regulation and high costs associated with its remediation (Naidu, 2013; Yoshida et al., 2016).

Recently, engineered magnetic iron-based adsorbents for removing heavy metals from water received special interests due to their high specific surface area, less toxicity than other magnetic nanoparticles, and superparamagnetic properties (Ambashta and Sillanpää, 2010; Tombácz et al., 2015; Brigante et al., 2016; Su, 2017). Despite their efficiency and promising application in adsorbent separation, the key challenges for these iron-based materials lie on ensuring a cost-effective preparation method, addressing the aggregation issues and understanding their environmental fate (Xu et al., 2012; Su, 2017). To reduce the cost of synthesis and provide an environmentally friendly approach, magnetic adsorbents prepared from natural resources like biochar (Han et al., 2016), starch (Xiang et al., 2016) and clay minerals (Tian et al., 2016) were reported. However, the functionalization of magnetic composites with clay minerals is important to cater the challenges even better due to clays' easy availability, stability, low toxicity, and high affinity towards various water contaminants, such as pesticides, phenolic compounds, industrial dyes and heavy metals (Murray, 2006; Sarkar et al., 2012). In water treatment processes, magnetic-clay composites could also increase their contaminant adsorption efficiencies, and address issues related to

spent adsorbent separation, which is often encountered while using unmodified clays (Chen et al., 2016a). A huge focus was given previously towards the structural modification of magnetic clay nanocomposites for enhancing their adsorption efficacy (Pan et al., 2011; Tian et al., 2016). However, an assessment on the magnetic recyclability of the composites was rather inadequate. The fate and stability of magnetic particles in enduring the adsorption-desorption and recycling process has been scarcely studied. It is still unclear how the magnetic adsorbents evolve during the regeneration process and whether one can use those spent materials (after multiple cycles of reactions) for further removal of contaminants. The saturation magnetization (M_s) and magnetic coercivity (H_c) are important parameters for the environmental remediation application of magnetic adsorbents. The M_s and H_c, respectively, represent the magnetic strength and the ability of a magnetic material to resist de-magnetization. While a high M_s value indicates a strong magnetic interaction, a low magnetic coercivity means the material would be readily separated (precipitated) from the suspension upon exposure to an external magnetic field. The separated material can then be re-dispersed as a colloidal suspension once the external magnetic field is removed. Superparamagnetic materials have a negligible remanence and coercivity value that allow a rapid response to the applied external magnetic field. This is desirable for an efficient magnetic separation of spent adsorbent (Mahdavian and Mirrahimi, 2010).

In addition, understanding the clay's role in preserving the magnetic sustainability of the composite requires careful attention for endowing the material's practical application in water treatment. Therefore, this research attempts to understand the clay-iron oxide structural integration and how they cooperatively contribute in the Pb(II) adsorption and regeneration studies. The influence of desorbing agent and magnetic recyclability were studied through the measurement of magnetic properties, structural morphology and analytical approaches. The broader aim of this research is to develop a magnetic clay composite as a tool for remediating

heavy metals from contaminated wastewaters. Palygorskite, an abundant clay mineral in Australia, was used in this study instead of more commonly used smectite. Natural palygorskite is inexpensive (costs approximately US$0.20 kg^{-1}), has elongated chain or lath-like particles, and contains high specific surface area suitable for the preparation of adsorbents and barrier materials (Murray, 2006).

2. Materials and methods

2.1 Materials and reagents

Palygorskite originating in Western Australia was purchased from Hudson Resource Pty. Ltd., Australia, lead (II) nitrate ($Pb(NO_3)_2$) and ammonium hydroxide (NH_4OH, 25% v/v) from Fisher Scientific (United Kingdom), iron (III) chloride hexahydrate ($FeCl_3.6H_2O$) from Chem-Supply (Australia), iron (II) chloride tetrahydrate ($FeCl_2.4H_2O$) from Sigma-Aldrich (Germany), and ethylenediaminetetraacetic acid disodium salt (EDTA- Na_2) from Sigma-Aldrich (United States). All other reagents were of analytical or laboratory grade.

2.2 Preparation of palygorskite-iron oxide (Pal-IO) nanocomposite

A co-precipitation method (Pan et al., 2011) with some modifications was used to prepare the palygorskite-iron oxide nanocomposite (Pal-IO). An initial mass ratio of 2:1 of palygorskite:iron oxide was chosen. $FeCl_3.6H_2O$ (4.72 g) was dissolved in 180 mL Milli-Q water (resistivity ≥ 18 MΩ.cm) followed by the addition of 4.2 g palygorskite (Pal) into the solution. The Pal-Fe^{3+} aqueous suspension was ultra-sonicated for 30 min and transferred to a 3-necked bottle with continuous mixing for 3 h at 25°C. Then $FeCl_2.4H_2O$ (1.72 g) was added into the above suspension under continuous N_2 flow (50 mL min^{-1}). The temperature was increased to 80°C and then 10 mL of NH_4OH (25% v/v) was added drop-wise to the Pal-Fe^{3+}-Fe^{2+} suspension with vigorous stirring for 30 min. The black precipitate product (Pal-IO)

was separated via centrifugation and washed thoroughly with Milli-Q water and ethanol until the pH of the supernatant became neutral (~pH 7). The Pal-IO precipitate was dried at 110°C for 3 h, grinded with pestle and mortar, and sieved to obtain particle size <90 μm. For comparison purpose, iron oxide (IO) was also synthesized using the same procedure without the addition of palygorskite.

2.3 Material characterization

The surface morphology was examined by using a FEI Quanta 450 FEG Environmental Scanning Electron Microscope (SEM) at High Vacuum (HV) mode using an Everhart-Thornley detector. The sample was carbon coated (30 nm) using a QUORUM Q150T E Carbon Coater. The Transmission Electron Microscope (TEM) images were collected using a JEOL JEM-2100F-HR transmission electron microscope with accelerating voltage of 200 kV. The powder X-ray Diffraction (XRD) patterns were collected on a PANalytical Empyrean X-ray diffractometer using CuK_{α} radiation (λ = 1.5406 Å) operating at 40 mA and 40 kV with a step size of 0.0130. The patterns were recorded from 9 to 99° 2θ by using a 0.25° fixed divergence slit and 0.50° anti-scatter slit. For the Fourier Transform Infra-Red (FTIR) analysis, a 1:200 (w/w) ratio of sample: KBr was used for the pallet preparation. The spectra were collected using an Agilent Cary 600 series spectrometer (Agilent Technologies) in the range of 4000–400 cm^{-1} by the co-addition of 16 scans with a resolution of 8 cm^{-1}.The specific surface area (SSA) and pore size distribution were determined by BET (Brunauer–Emmett–Teller) and BJH (Barrett-Joyner-Halenda) methods, respectively, through N_2 gas adsorption-desorption experiments on a Micromeritics Gemini 2380 Surface Area Analyzer. The zeta potential values of the adsorbents in aqueous suspension (0.01% m/v) were measured on a zeta potential analyzer (Nicomp™ 380 ZLS, USA). The thermo gravimetric analysis (TGA) was conducted on a Mettler Toledo Thermogravimetric Analyzer (TGA/DSC

1 model) equipped with STAR^e system with heating rate of 10°C min^{-1} from 25 to 950°C under N_2 environment (50 mL min^{-1}). Magnetic measurement was conducted using a Vibrating Sample Magnetometer (VSM) supplied by Princeton Measurement Corporation (MicroMag^{TM} Model 3900 Series). The measurement was conducted in triplicates at 27°C with applied field of 1 Tesla and averaging time of 100 to 200 ms.

2.4 Adsorption experiments

Aqueous solutions of Pb(II) with required concentrations (10, 20, 50, 100, 200, 300 and 500 mg L^{-1}) were prepared by dissolving $Pb(NO_3)_2$ in Milli-Q water followed by subsequent dilutions. These concentrations were within the typical Pb concentration ranges found in contaminated acid mine drainage water (Lottermoser, 2010). Batch adsorption experiments of palygorskite-iron oxide nanocomposite (Pal-IO), pristine palygorskite (Pal) and iron oxide (IO) were conducted (experimental condition: 25°C, pH 5, 5 g L^{-1} adsorbent loading, 150 agitations per min, contact time of 12 h) in capped polypropylene tubes at a pre-determined Pb(II) concentration. The kinetic adsorption experiments were conducted under similar conditions, with 1 mL aliquot being taken out from the suspension at pre-determined time intervals for Pb(II) concentration measurement.

After each completed adsorption reaction, the supernatant of Pal-IO and IO were retrieved by the magnetic separation process (using a bar magnet) followed by filtration through a 0.45 μm membrane filter. For palygorskite, the suspension was centrifuged at the relative centrifugal force (RCF) of 1512 x *g* for 10 min before the membrane filtration. The initial and equilibrium concentrations were determined using an Inductively Coupled Plasma Optical Emission Spectrometer (ICP-OES) (Perkin Elmer, Optima 5300V) in duplicates and the mean value was reported. Adsorption of Pb(II) on the walls of the polypropylene tube was negligible.

The amount of Pb(II) adsorbed onto the adsorbent was calculated using Eq. 1:

$$q_e = \frac{(C_i - C_e)\,V}{m} \quad \text{.....Eq. 1}$$

where, q_e is the amount of metal adsorbed at equilibrium (mg g^{-1}), C_i and C_e are the initial and equilibrium metal concentrations (mg L^{-1}), respectively, V is the volume (L) of the solution, and m is the mass (g) of the adsorbent.

2.5 Adsorbent regeneration studies

The Pb(II)-loaded adsorbent obtained from the adsorption experiment with 100 mg L^{-1} Pb(II) was first separated from the supernatant. The spent adsorbent was then dispersed (5 g L^{-1} loading rate) into either EDTA-Na_2 or HCl solutions (both 0.01 M) and agitated (150 agitations per min) for 30 min on a reciprocating shaker. Afterwards the adsorbent was thoroughly washed (3 times) with Milli-Q water until the pH of the wash-out water reached the range of 6.0–6.5 and no Pb(II) was detected in the wash-out solution as determined by ICP-OES. Then, the adsorbent was re-used for the subsequent adsorption cycle as described previously (Section 2.4). The desorption percentage was calculated by using Eq. 2:

$$\text{Desorption}(\%) = \frac{\text{Amount of Pb desorbed}}{\text{Amount of Pb adsorbed}} \times 100 \quad \text{.....Eq. 2}$$

3. Results and discussion

3.1 Characterization of Pal-IO nanocomposite

The morphology of bare iron oxide (IO) particles was almost spherical, homogenous and fairly well dispersed (Fig. 1a). The formation of iron oxide, for example, magnetite (Fe_3O_4), usually involves the nucleation and growth process, but recently a rapid agglomeration of the primary particles was also reported (Baumgartner et al., 2013). In the magnetic palygorskite (Pal-IO), the spherical iron oxide particles were observed to accumulate along the fiber and

200 platy edge of the palygorskite (Fig. 1b and c). The precursor iron (Fe^{3+}/Fe^{2+}) supplied during
201 the synthesis reaction was assumed to diffuse along the negatively charged plane of
202 palygorskite. Since the palygorskite holds a permanent negative charge, the Coulombic
203 attraction would have driven the electrostatic interaction between the surface functional
204 groups of palygorskite and the oppositely charged Fe^{3+}/Fe^{2+} ions (Tombácz et al., 2001; Lee
205 et al., 2010) forming a crosslinking reaction between the clay surface and Fe (Chen et al.,
206 2016b). Thus, upon alkali addition (concentrated OH^-), the nucleation, growth and
207 agglomeration of iron oxide would occur primarily along the surface of palygorskite. The
208 estimated dimension of iron oxide particles in Pal-IO obtained through TEM images (Fig. 1c
209 and d) was between 15 to 25 nm. Although the fibrous particles of palygorskite were
210 randomly oriented, they still existed as bundles (approximate width: 100 to 130 nm) having
211 individual tubules (20 to 30 nm width) placed parallel to each other (Fig. 1c and 1d). These
212 observations showed that the strong interactions among the palygorskite particles were
213 preserved and their fiber-bundle design ensured a strong adherence towards the iron oxide
214 nanoparticles.
215

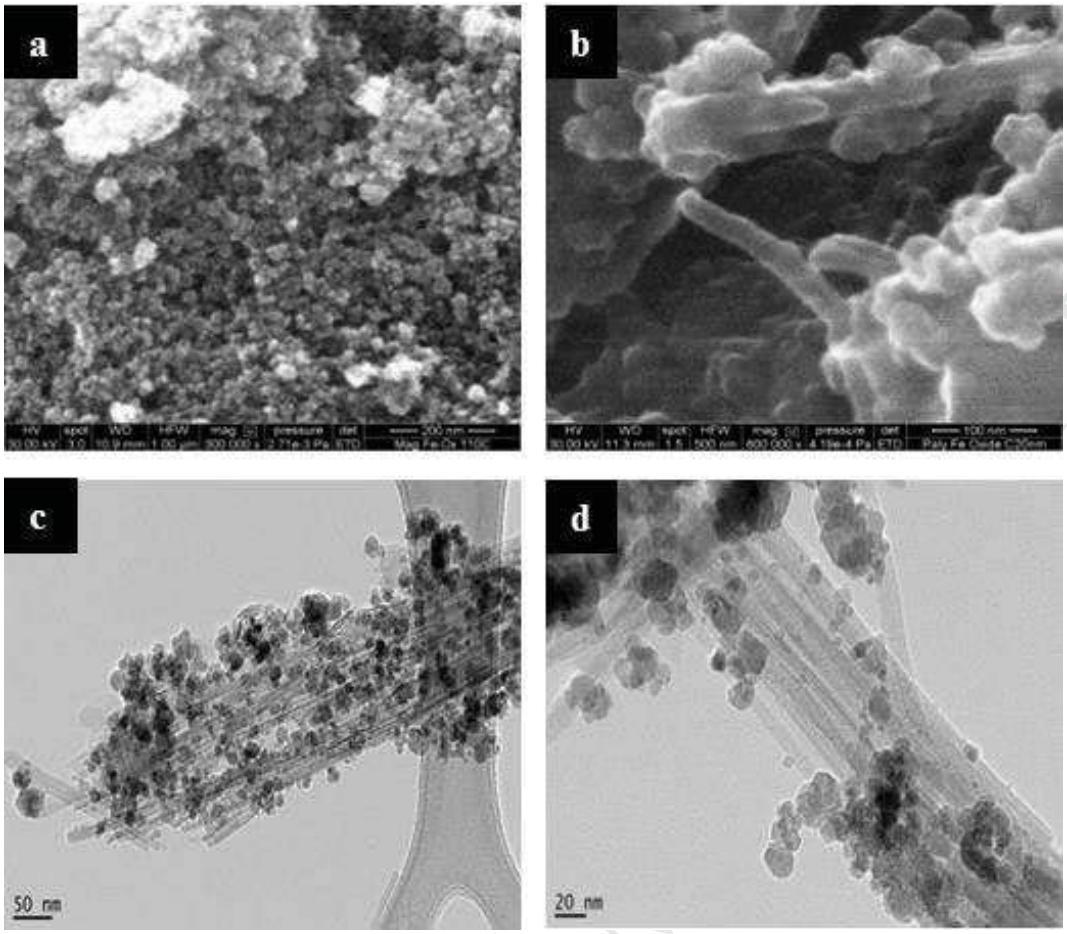

Fig. 1: SEM (a-b) and TEM (c-d) images of iron oxide and palygorskite-iron-oxide nanocomposite; (a) iron oxide, (b-d) palygorskite-iron oxide nanocomposite

The specific surface area (SSA) of the nanocomposite (Pal-IO) was significantly higher (99.8 $m^2 g^{-1}$) than the pristine materials (49.4 and 72.6 $m^2 g^{-1}$ for Pal and IO, respectively). All the materials exhibited a type IV adsorption profile (IUPAC classification) corresponding to mesoporous materials (Fig. 2a) (Sarkar et al., 2015). Both the palygorskite and Pal-IO had a hysteresis loop (H3 type) associated with the parallel plates or slit-shape pores (Sarkar et al., 2015), while iron oxide (IO) exhibited a H1 type loop with almost a consistent pore volume distribution (Fig. 2b). The increase of surface area and pore volume in Pal-IO was due to the leaching of cations and impurities from the clay matrix in the acidic $Fe^{3+/}Fe^{2+}$ suspension (pH 2.2) (Section 2.2) that caused the rearrangement of clay mineral's porosity.

229

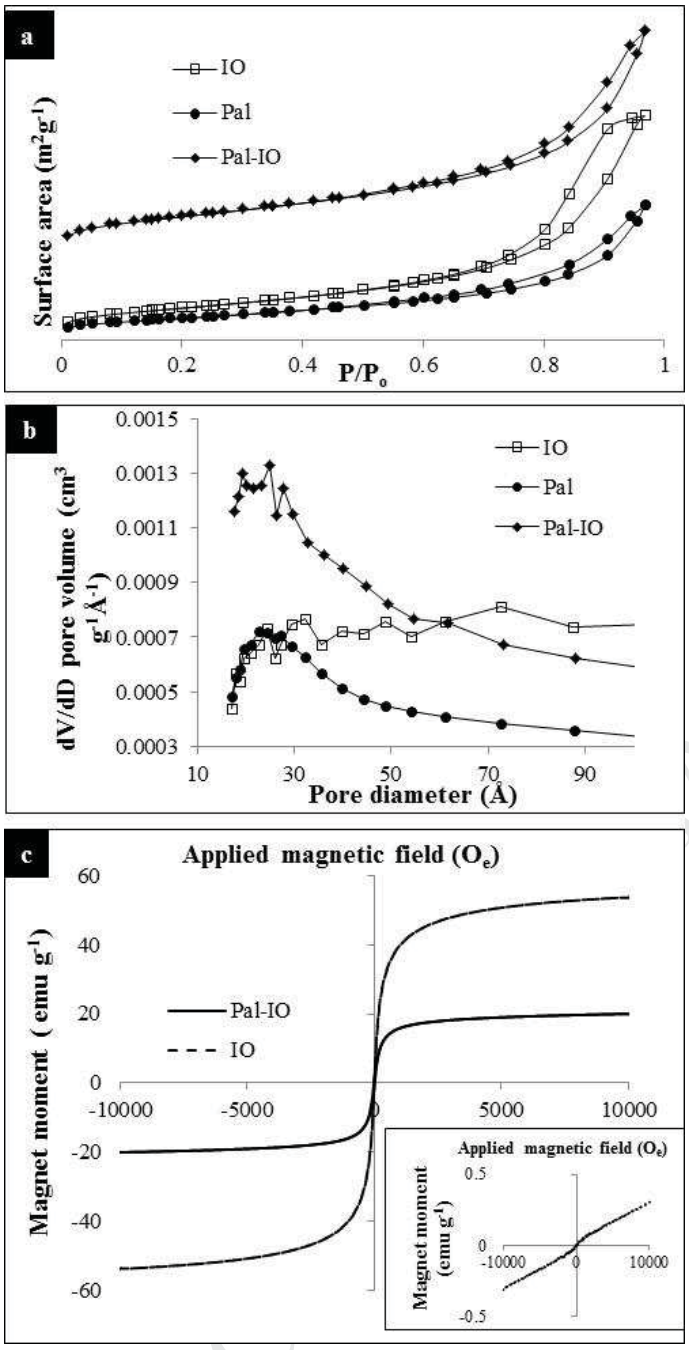

230

231 Fig. 2: N_2 adsorption-desorption isotherms (a), BJH pore size distribution (b), and

232 magnetization curve (c) of palygorskite (Pal), iron oxide (IO) and palygorskite-iron oxide

233 nanocomposite (Pal-IO). Inset in Fig.2 (c) is for palygorskite

234

235 The complete separation of Pal-IO from the suspension using Alnico magnet bar was

236 generally fast (within 60 to 120 sec). The plot of M_s (emu g^{-1}) against the applied magnetic

field (O_e) of the iron oxide and Pal-IO produced an "S" shaped magnetic hysteresis loop with a near zero remanence and coercivity (Fig. 2c), which confirmed a superparamagnetic characteristic of the material (Tsuzuki et al., 2011). The bare iron oxide (IO) had the M_s value of 54.2 ± 2.5 emu g^{-1}. The slightly lower M_s value of the synthesized IO as compared to the bulk magnetite (Fe_3O_4) or maghemite (γ-Fe_2O_3) (92 and 87 emu g^{-1}, respectively) could be due to the formation of a thin layer of magnetically disordered shell on the nanoparticle surface (Tsuzuki et al., 2011). A M_s value of 20.2 ± 2.3 emu g^{-1} was recorded for the Pal-IO nanocomposite, which was higher than the recommended value for the conventional magnetic separation of a spent adsorbent (16.3 emu g^{-1}) (Ma et al., 2005). Meanwhile, palygorskite (Fig. 2c) was almost diamagnetic due to an extremely small magnetic saturation. The measured H_c for palygorskite and Pal-IO was 21.4 ± 3.1 and 18.8 ± 0.1 O_e (k A m^{-1}), respectively. The bare IO had a negligible H_c value. The appreciable decrease in the M_s value of Pal-IO as compared to the bare IO was due to the contribution of the nonmagnetic substance (palygorskite) (Liu et al., 2014).

The characteristic XRD reflections of palygorskite were observed at 2θ = 8.5° (10.39 Å), 19.6° (4.52 Å) and 24.9° (3.57 Å) together with the presence of kaolinite at 2θ = 12.3° (7.19 Å) and quartz at 2θ = 20.8° (4.27 Å) and 26.4° (3.37 Å) (Fig. 3a) (Sarkar et al., 2015). The sharp reflection at 2θ = 30.8° (Fig. 3a) was designated to dolomite (calcium magnesium carbonate) which was an impurity in the clay mineral sample. The synthesized iron oxide showed reflections at 2θ positions of 30.1°, 35.5°, 43.1° 53.4°, 57.0° and 62.6° (Fig. 3a) which respectively corresponded to (220), (311), (400), (422), (511) and (440) reflection planes of magnetite (Pan et al., 2011; Chen et al., 2016b). These diffraction patterns were in good agreement with the International Center for Diffraction Data (ICDD) reference pattern of magnetite (Fe_3O_4) (ICDD File No. 04-008-8146). In Pal-IO (Fig. 3a), a slight broadening of the (100) reflection of palygorskite (2θ = 8.5°) occurred, which suggested a mild reduction

in the palygorskite crystallinity due to their interaction with the iron oxide. Nevertheless, the presence of all the characteristic palygorskite and Fe_3O_4 reflections in the Pal-IO diffraction pattern (Fig. 3a) signified the successful deposition of the magnetic nanoparticles on the palygorskite in Pal-IO.

In FTIR spectrum of palygorskite, (Fig. 3b), the –OH stretching vibration of Mg/Fe–OH (3695 cm^{-1} and 3545 cm^{-1}), Al_2-OH (3618 cm^{-1}), Al-Al-OH (910 cm^{-1}) and Al-Mg-OH (880 cm^{-1}) represented the characteristic bands of this clay mineral (Madejová and Komadel, 2001; Suárez and García-Romero, 2006). The silica structural confirmation appeared at 1030 cm^{-1} (Si-O-Si asymmetric stretching), 790 cm^{-1} (Si-O-Si symmetric stretching) and 471 cm^{-1} (Si-O-Si bending) bands. Meanwhile, the band at 578 cm^{-1} in the spectra of IO (magnetite) (Fig. 3b) corresponded to the stretching vibration of Fe-O together with a small maghemite (γ-Fe_2O_3) band at 628 cm^{-1} (Namduri and Nasrazadani, 2008). The signature band positions that corresponded to the palygorskite and iron oxide were present in the FTIR spectrum of Pal-IO (Fig. 3b). However, the bands at 1450 cm^{-1} (C=O, carbonate impurity) (Gunasekaran et al., 2006) , 3545 cm^{-1} (Mg-OH stretching), and 880 cm^{-1} (Al-Mg-OH bending) were diminished.

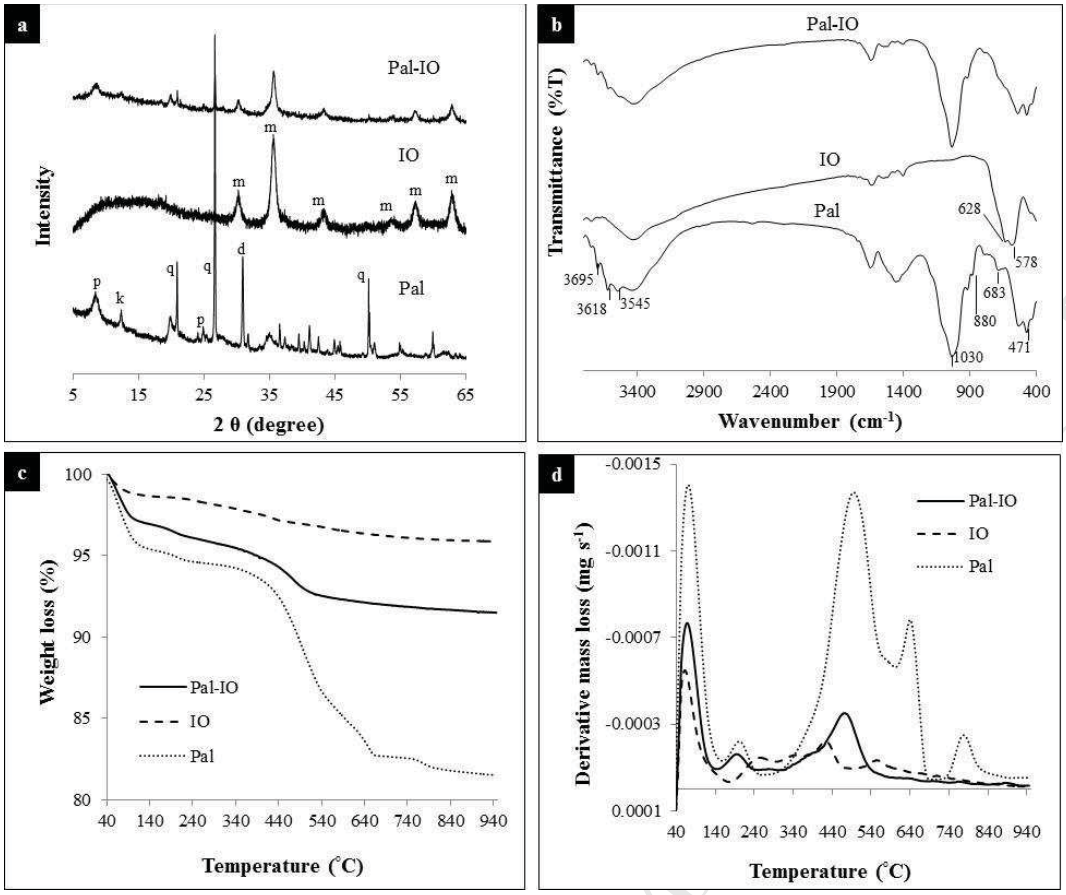

Fig. 3: Characteristic features of palygorskite (Pal), iron oxide (IO) and palygorskite-iron oxide nanocomposite (Pal-IO): (a) XRD patterns, (b) FTIR spectra, (c) TGA profiles and (d) DTGA profiles. (p = palygorskite, k = kaolinite, q = quartz, d = dolomite, m = magnetite)

In TGA, the magnetic nanocomposite (Pal-IO) displayed an 8.5% weight loss in the temperature range from 40 to 950°C (Fig. 3c) against 4% and 18% weight loss by bare iron oxide (IO) and pristine palygorskite (Pal), respectively. The palygorskite showed five pronounced endothermic weight loss steps (Fig. 3d): step 1 (4% loss with a peak at 65°C), step 2 (0.73% loss with a peak at 200°C), step 3 (9.8% loss with a peak at 503°C), step 4 (1.97% loss with a peak at 635°C) and step 5 (0.94% loss with a peak at 760°C). The step 1 was ascribed to the loss of surface-adsorbed and some zeolitic water. The step 2 was assigned to the elimination of the remaining zeolitic water. The dehydration and loss of the bound water were assigned to step 3 (Cheng et al., 2011). The step 4 and step 5 could possibly

correspond to the dolomite or calcite decarbonation (Guggenheim and Groos, 2001; Cheng et al., 2011) and dehydroxylation of structural Mg-OH groups (Frost and Ding, 2003), respectively. In Pal-IO, only three weight loss steps were observed (peaks at 48°C, 180°C and 465°C) (Fig. 3d), which corresponded to the elimination of various types of waters either from the palygorskite exterior surface or internal structure, as explained above for pristine palygorskite. The disappearance of peaks at step 4 and 5 in Pal-IO thermogram suggested dolomite/calcite decarbonation and dehydroxylation, respectively (as also observed in case of pristine palygorskite).

Overall findings in the characterization studies confirmed the integration of the pristine material (palygorskite and iron oxide) in Pal-IO. The composite showed better structural properties like higher SSA, more thermally stable, and better magnetic responsiveness. A successful removal of carbonate impurity from the palygorskite (as confirmed by XRD, FTIR and TGA) was achieved as a consequence of its dispersion in an acidic Fe^{3+}/Fe^{2+} solution during the synthesis process. This protocol therefore was able to exclude the conventional pre-treatment steps of clay minerals (using inorganic acids like HCl or HNO_3) for a greener and cost-effective synthesis.

3.2 Adsorption of Pb(II)

3.2.1 Adsorption isotherm

The theoretical interpretation of the relationship between adsorption capacity and equilibrium concentration was done using two well-established isothermal models, namely the Langmuir and Freundlich model (Supporting Information: S1). In a preliminary experiment, the maximum Pb(II) removal by Pal-IO was achieved at pH 5 (Supporting Information: SI Fig. 1), thus this pH value was used throughout the isothermal studies. The pH 5 is also a typical pH associated with contaminated waters from gold and coal mining activities (Lottermoser,

2010). The adsorption isotherm data of Pal-IO and Pal (Fig. 4a) exhibited a very sharp "elbow" at the equilibrium concentration (C_e) less than 50 mg L^{-1} (which corresponded to the initial concentration of 10 to 200 mg L^{-1}). It was followed by a steady increase up to C_e of 100 mg L^{-1}. The shape resembled an H type (Giles classification) isotherm associated with an almost complete adsorption due to a very high affinity of solute (Pb(II)) towards the adsorbent (Giles et al., 1960).

The adsorption data for IO, Pal and Pal-IO best fitted to the Langmuir model (regression coefficient, $R^2 > 0.98$; $p < 0.05$) (Table 1 and Supporting Information: SI Fig. 2), which suggested a monolayer adsorption on the active sites of each adsorbent. The palygorskite (Pal) showed the highest monolayer saturation capacity (q_{max}); Pal-IO had the highest K_L value which demonstrated a stronger interaction of their active sites (e.g., Al-O^-, Si-O^- or Fe-O^-) with Pb(II). These findings were in accordance with the higher n value (favorability of adsorption) for Pal-IO derived from the Freundlich isothermal model (Table 1). The calculated R_L values at all concentration for each adsorbent recorded a value between 0 and 1 (Supporting Information: SI Table 1), which again signified a favorable adsorption reaction.

Table 1: Isothermal and kinetic model fitting parameters for the adsorption of Pb(II) on palygorskite, iron oxide and palygorskite-iron oxide nanocomposite (at 25°C, under 150 agitation min^{-1} with 5 g L^{-1} adsorbent loading)

Model	Parameter	Palygorskite	Iron oxide	Palygorskite-iron oxide nanocomposite
Isothermal models				
Langmuir	q_{max} (calculated) (mg g^{-1})	50.8	6.00	26.7
	K_L (L mg^{-1})	0.136	0.040	0.303

	q_{max} (experimental) (mg g^{-1})	49.2	6.10	26.6
	R^2	0.9992	0.9896	0.9995
Freundlich	K_F (L g^{-1})	6.852	1.097	6.566
	n	2.30	3.43	3.47
	q_{max} (calculated) (mg g^{-1})	37.3	1.80	16.9
	R^2	0.8762	0.9831	0.8588
Kinetic models				
Pseudo first order	k_1 (min^{-1})	[a]NS	NS	0.035
	q_{max} (calculated) (mg g^{-1})	NS	NS	2.8
	q_{max} (experimental) (mg g^{-1})	NS	NS	4.1
	R^2	NS	NS	0.8947
Pseudo second order	k_2 (g mg^{-1} min^{-1})	NS	NS	0.012
	q_{max} (calculated) (mg g^{-1})	NS	NS	4.4
	q_{max} (experimental) (mg g^{-1})	NS	NS	4.1
	R^2	NS	NS	0.9945
Intra particle diffusion	k_i (mg g^{-1} $min^{0.5}$)	NS	NS	0.2071
	R^2	NS	NS	0.8249

[a] NS = not studied.

The adsorption profiles of the pristine palygorskite and iron oxide were useful to understand the relationship and contribution of each individual component towards the adsorption characteristic of the nanocomposite. In an aqueous system, iron oxide (magnetite) would hydrate to form a Fe-OH coating layer surrounding the particles. Depending on the pH of the aqueous solution, the Fe-OH layer could develop either a positive or negative surface charge with the available H^+ or OH^- (Illés and Tombácz, 2006). As the isoelectric point (IEP) of IO was 5.6 (Supporting Information: SI Fig. 3), at the given experimental conditions (pH 5), the IO had a positively charged surface below pH 5.6. Therefore, IO had less affinity to Pb(II), which further explained its poor adsorption capacity (Table 1). Furthermore, the bare iron oxide nanoparticles were prone to aggregation due to their high surface energy that later reduced the Pb(II) accessibility towards active sites (Chen et al., 2016a). Meanwhile, the pristine palygorskite showed a high adsorption capacity owing to their negative surface charge that resembled the abundance of active sites for interaction with Pb(II). In general, the adsorption of cationic metal on clay minerals can occur though both specific and non-specific adsorption. The non-specific adsorption (outer sphere complexation) involves the cation exchange reaction within the interlayer, while the specific adsorption (inner sphere complexation) often occurs through the silanol and aluminol groups at the edges of clay particles (El-Bayaa et al., 2009).

In the case of Pal-IO, the nanocomposite showed an appreciable decrease in the maximum adsorption capacity (q_{max}) in comparison to the pristine palygorskite (Pal) (Table 1). However, when considering the K_L, n and R_L values (Table 1 and Supporting Information: SI Table 1), Pal-IO showed a stronger affinity towards Pb(II) as compared to both Pal and IO. As shown in the gray scale area (Fig. 4b), at initial Pb(II) concentration between 10 to 200 mg L^{-1}, Pal-IO showed a higher adsorption capacity than Pal and IO (up to 63% and 86% more, respectively). The greater adsorption capacity was contributed by the higher pore

364 volume of Pal-IO as compared to Pal (Fig. 2b), which allowed more Pb(II) diffusion towards
365 the active sites of the nanocomposite. In addition, the synergic contribution of the active sites
366 from both parent materials, e.g., silanol (Si-OH) and aluminol (Al-OH) functional groups in
367 Pal and Fe-O^- in IO, could possibly enhance the composite's affinity towards the heavy metal
368 cation. Clay minerals like palygorskite may have variable surface charges constituted of Si-
369 OH and Al-OH groups that are capable to adsorb metal cations through inner-sphere
370 complexation depending on the system pH (El-Bayaa et al., 2009). Meanwhile, Fe-O^- could
371 act as a Lewis base by coordinating with Pb^{2+} to form inner-sphere complexes (Kumari et al.,
372 2015). At the working pH 5, partial protonation of Fe-O^- to Fe-OH could also lead to both
373 inner- and outer-sphere complexations with Pb^{2+} (Kumari et al., 2015).
374

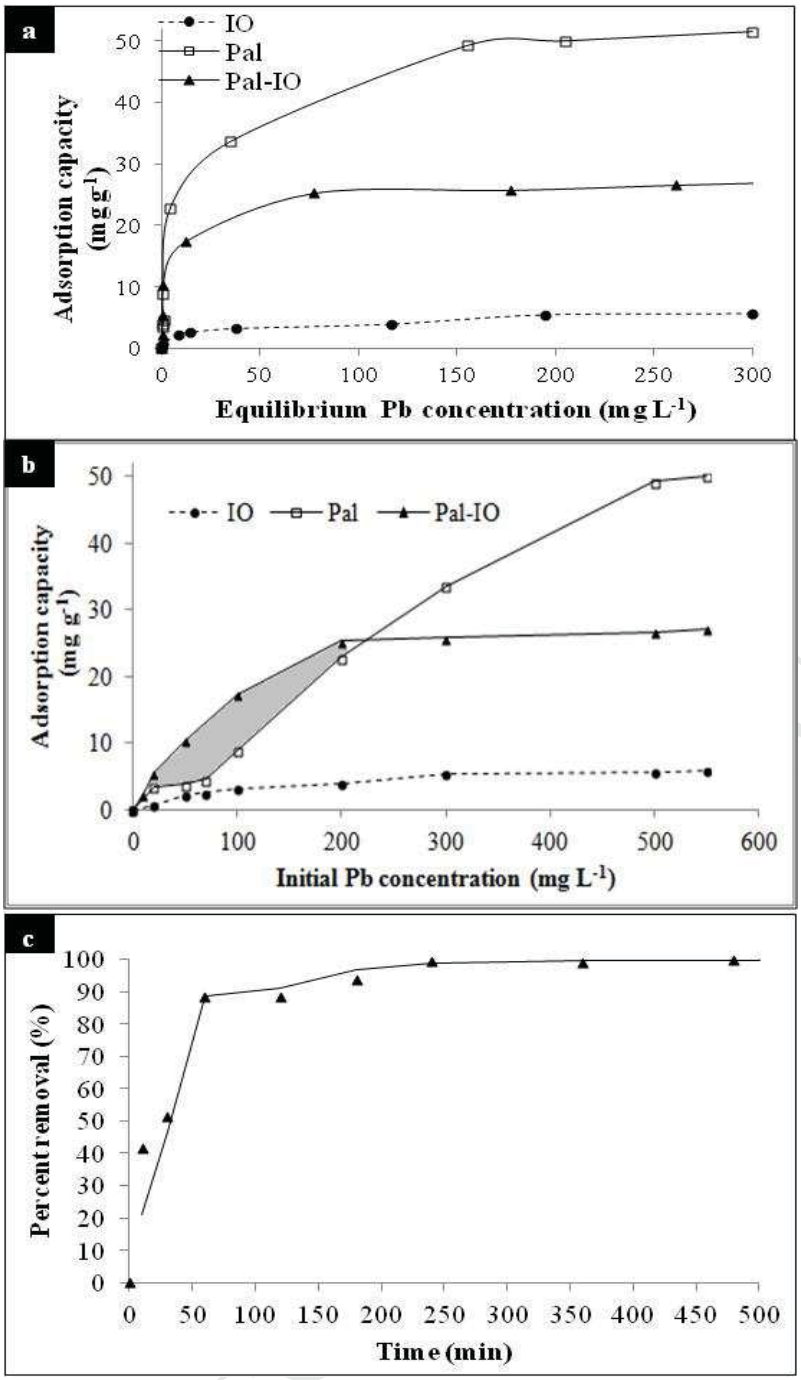

375

376 Fig. 4: Adsorption of Pb(II) on palygorskite (Pal), iron-oxide (IO) and palygorskite-iron

377 oxide nanocomposite (Pal-IO): (a) adsorption isotherms, (b) effect of initial Pb(II)

378 concentration on the adsorption capacity, and (c) effect of reaction time on Pb(II) removal by

379 Pal-IO at initial Pb(II) concentration of 50 mg L^{-1} at 25°C with 150 agitations min^{-1} and 5 g

380 L^{-1} loading

381

382 3.2.2 Adsorption kinetics

383 The pseudo-first order, pseudo-second order and intra-particle diffusion models were chosen
384 to establish an understanding of the adsorption kinetics (Supporting Information: SI 2). The
385 kinetic plot (Fig. 4c) showed that 42% of Pb(II) was removed in the first 10 min of the
386 experiment, double (89%) at 60 min of reaction, and full equilibrium (~100%) after 240 min.
387 The relatively faster reaction rate indicated a high affinity of Pb(II) towards the active sites of
388 Pal-IO, in accordance with the observed H type adsorption isotherm (Section 3.2.1). To
389 ensure a complete equilibrium at various initial concentrations, a 12 h equilibration time was
390 therefore necessary. Among the three kinetic models applied, the pseudo-second order model
391 most suited the adsorption data ($R^2 = 0.9945$; $p < 0.05$), where the q_{max} value was consistent
392 with the experimental value (Table 1). The fitness of the pseudo-second order model
393 indicated that the rate limiting step of Pb(II) adsorption occurred through chemisorption (Ho
394 and McKay, 1999).

395

396 3.3 Desorption studies

397 3.3.1 Effect of desorbing agent

398 At given experimental conditions, the type of desorbing agent and pH was found to
399 significantly influence the desorption of Pb(II) from Pal-IO (Table 2). The negligible Pb(II)
400 desorption in Milli-Q water (pH 6.2) reflected the high retention ability of Pb(II) by the
401 nanocomposite. In acidic solutions, the lower pH could enhance the metal desorption due to
402 the leaching of cations (e.g., Fe). At 0.01 M concentration, HCl showed a higher release of
403 Pb(II) compared to HNO_3, but the trend was reversed at 0.1 M concentration. The chloride
404 ions in HCl were able to form effective complexes with Pb(II) to assist the desorption process
405 (Kim et al., 2011). However, at a higher acid concentration, HNO_3 might cause the oxidation
406 of magnetite (Mandel et al., 2011) in Pal-IO that likely would disrupt the composite's

407 stability to hold Pb(II). The increase in pH of the acidic desorbing agent following the
408 desorption reaction also suggested a possible cation exchange between H^+ with Pb(II) at the
409 active sites (Huang et al., 2007).

410

411 Table 2: Desorption of Pb(II) from Pal-IO using various desorbing agents (standard error at
412 0.95 confidence level)

Desorbing agent	Initial pH	Final pH	Desorption (%)	Fe leached (%)
0.01 M HCl	1.96	2.21	89.2±7.23	0.57
0.1 M HCl	1.57	4.54	75.6±1.90	2.89
0.01 M NaOH	11.3	10.8	0.55±0.55	0.88
0.01 M NaCl	5.16	5.99	1.20±0.02	ND[b]
0.01 M NH_4OAc (ammonium acetate)	6.67	3.54	0.45±0.24	ND
Milli-Q water	6.20	6.47	0.78±0.23	ND
0.01 M HNO_3	1.80	4.48	72.0±1.25	0.42
0.1 M HNO_3	1.66	4.75	90.4±1.70	2.61
0.01 M EDTA-Na_2	8.90	4.62	95.0±3.14	0.78
0.1 M EDTA-Na_2	9.10	4.52	95.57±0.10	0.88

413

414 [b] ND = not detected.

Ammonium acetate is commonly used to determine the cation exchange capacity (CEC) of clay minerals where NH_4^+ can be easily exchanged with the cationic species present in the interlayer. A very small Pb(II) desorption by ammonium acetate in the desorption test indicated that, (i) Pb(II) might not be exchangeable with other cations at the interlayer region, and (ii) if Pb(II) was present in the interlayer, NH_4^+ might not be able to replace Pb(II) due to some steric hindrance of NH_4^+ tetrahedral configuration and larger ionic radii (1.48 Å) as compared to Pb(II) (1.32 Å) (Shahbazi et al., 2013). On the other hand, smaller cations like Na^+ (ionic radius of 0.95 Å) in NaCl might be easily exchangeable with Pb(II).

EDTA usually showed a higher metal desorption over inorganic acids due to its ability to form strong complexation (up to six coordination indexes) via the electron rich (amidogen and carboxylic) ligand groups (Huang et al., 2007). The recorded pH reduction (Table 2) signified the release of proton (H^+) from the hydroxyl groups within EDTA that were used up during Pb(II) complexation. Both 0.01 and 0.1 M EDTA-Na_2 showed a high Pb(II) desorption (more than 90%). In contrast to HCl and HNO_3, the amount of Fe leached out from Pal-IO using EDTA was negligible (4.41 mg L^{-1}; <1%) even at a 0.1 M concentration (Table 2). Considering the desorptive effectiveness of Pb(II) and economic perspective, 0.01 M EDTA-Na_2 was preferably the best desorbing agent. However, HCl might also have some advantages in terms of cheaper cost and availability. The percentage of Fe leached from Pal-IO by 0.01 M HCl and 0.01 M EDTA-Na_2 was only 0.57 and 0.78%, respectively (Table 2). Thus, the leached Fe was considered to have insignificant effect towards Pb(II) adsorption capabilities of the composite.

3.3.2 Regeneration of the adsorbent

439 The regeneration cycle of Pal-IO was carried out by using both EDTA and HCl as the
440 desorbing agent. For better clarification, the Pb(II) loaded Pal-IO, which was desorbed by
441 0.01 M EDTA-Na_2 and 0.01 M HCl, were assigned as Pal-IO-EDTA and Pal-IO-HCl,
442 respectively. The Pb(II) removal during desorption with EDTA was reduced by 21.3 and
443 31.2% after the second and third cycle, respectively (Fig. 5a). A small portion of Pb(II) might
444 strongly bind to the nanocomposite as indicated by the 97.5% desorption using EDTA in the
445 first cycle (Fig. 5a). By making an assumption that 26.6 mg g^{-1} Pb(II) loading (calculated q_{max}
446 based on the Langmuir model; Table 1) would make 100% monolayer coverage, the initial
447 concentration of 100 mg L^{-1} would make 65% coverage at each adsorption cycle. Thus,
448 during the second and third cycle the active sites became extensively occupied with the
449 freshly supplied Pb(II) together with the remaining Pb(II) entrapped in the prior cycle(s). This
450 factor thus resulted in a lower Pb(II) adsorption in the subsequent cycles. The findings were
451 also in parallel with a slight increase in Pb(II) desorption at the second and third cycle
452 (Fig.5a). The excess build-up of Pb(II) within the nanocomposite could stimulate its release
453 during desorption as the saturated nanocomposite could no longer hold the additional Pb(II).
454 Meanwhile, the adsorption-desorption cycle of Pal-IO showed a similar pattern when using
455 HCl as the desorbing agent. However, the adsorption by Pal-IO-HCl was greatly reduced
456 from 97% (first cycle) to 50 and 48% in the second and third cycle, respectively.
457

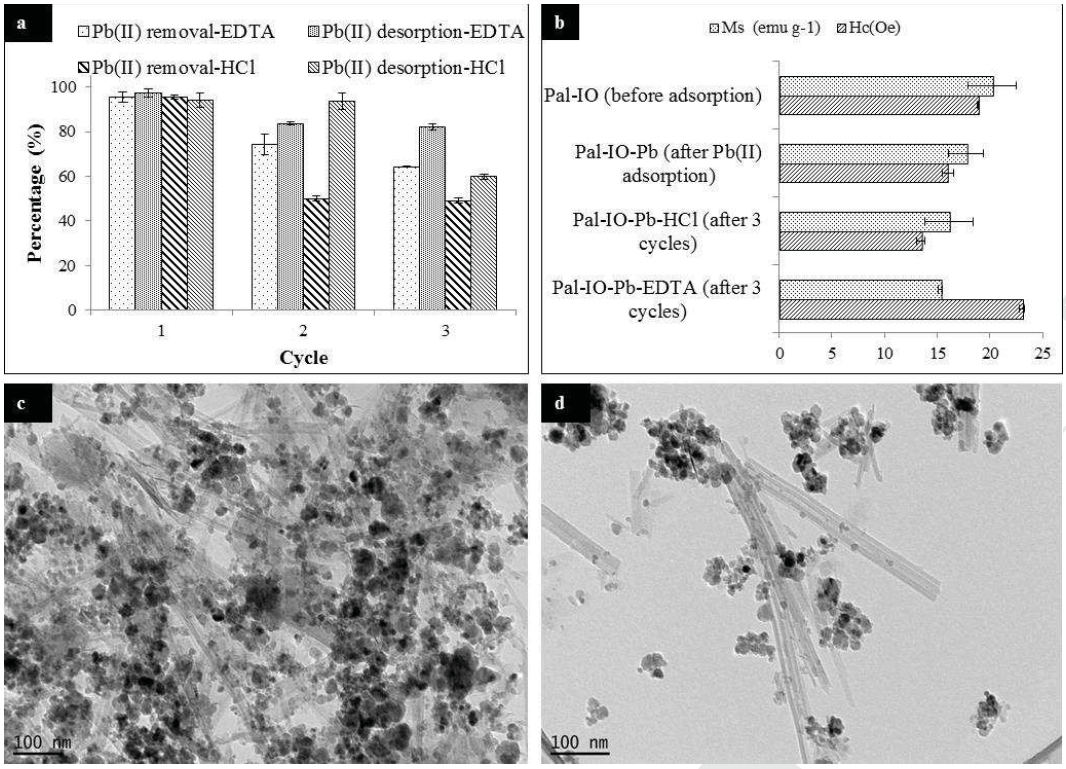

Fig. 5: Comparison on Pb(II) adsorption and desorption (in percentage) by Pal-IO using EDTA (Pal-IO-EDTA) and HCl (Pal-IO-HCl) as the desorbing agent (a), magnetic properties of fresh and spent Pal-IO nanocomposite (b), and TEM images of Pal-IO-EDTA (c) and Pal-IO-HCl (d) nanocomposite after three regeneration cycles. Error bars represent the standard error at 0.95 confidence level.

The findings of the adsorption-desorption cycles were correlated with the changes observed in the magnetic properties of the spent Pal-IO at three different stages; (i) before Pb(II) adsorption, (ii) after Pb(II) adsorption, and (iii) after three adsorption-desorption cycles (Fig. 5b). After third regeneration cycle, Pal-IO-EDTA showed a higher magnitude of coercivity (H_c) than Pal-IO-HCl (Fig. 5b), which suggested that the solid aggregation was greater in the earlier material. It was reported that EDTA was able to produce strong complexes with iron (hydr)oxide (Fe-EDTA complexes) that simultaneously promoted their dissolution from Pal-IO due to weakened surface Fe-O bonds (Norén et al., 2009). The Fe-EDTA complexes

might readsorb on the Fe-O surface as previously found in goethite (α-FeOOH) (Norén et al., 2009). Therefore, the dissolution-readsorption of Fe-EDTA complexes could possibly occur through the embedded iron oxide nanoparticles within the Pal-IO nanocomposite, which later influenced the coercivity due to the changes in surface properties and shape anisotropy (Issa et al., 2013). Each material showed almost equivalent magnetic susceptibility (M_s) with a reduction of 4.0 to 4.8 from the original value (20.2 emu g^{-1}) (Fig. 5b). A minor loss of M_s indicated that iron oxide nanoparticles were strongly adhered to the palygorskite. This conclusion was supported by the TEM images of the spent Pal-IO (Fig. 5c and 5d). In Pal-IO-EDTA (Fig. 5c), majority of the iron oxide nanoparticles were still closely adhered to the palygorskite bundles even after the three consecutive regeneration cycles. In contrast, the palygorskite fibers were seen detached from their bundles in Pal-IO-HCl (Fig. 5d) accompanied by some scattered iron oxide nanoparticles. Therefore, it could be concluded that the acidic treatment for desorption had the potential to disaggregate the particles in spent Pal-IO nanocomposite to make it more loosely packed. This observation was useful to explain the reduction in Pb(II) adsorption in the regeneration profile of Pal-IO-HCl. Acid attack on clay minerals could cause hydrolysis and dissolution of octahedral layers at the edges. Thus, repeated desorption of spent Pal-IO with HCl would possibly expedite palygorskite's dissolution, which might lead to disaggregation of the crystal bundles of the clay mineral. Additionally, some entrapped H^+ (from HCl) within the Pal-IO matrix could reduce the availability of active sites for Pb^{2+}, and thus decrease the metal's adsorption in the next regeneration cycles. These hypotheses however require further investigation to prove. The overall findings demonstrated that the choice of desorbing agent influenced the magnetic recyclability and metal leaching from Pal-IO. For future prospective application of Pal-IO in waste water remediation, EDTA would be a more preferable desorbing agent over HCl, as also proposed previously (Udovic and Lestan, 2012).

498

499 3.3.3 Environmental implication

500 The superparamagnetic Pal-IO composite described in this study could be implemented for
501 remediating heavy metals from contaminated wastewaters in a treatment plant. Due to
502 advantages like low costs, simple preparatory steps, high specific surface area and large
503 adsorption capacities, Pal-IO is expected to be a promising material in removing Pb and other
504 heavy metals (e.g., Cr and Cd) from waste waters (Kumari et al., 2015). The Pb(II) removal
505 capacity of Pal-IO is comparable to some reported adsorbents, such as mesoporous magnetite
506 nanospheres (Brigante et al., 2016), functionalized mesoporous silica (Shahbazi et al., 2013),
507 and magnetic Fe_3O_4/halloysite composite (Tian et al., 2016). According to the existing
508 findings, the material might fit to treat wastewaters which contain a typical Pb(II)
509 concentration up to 200 mg L^{-1}. However, further research is needed to assess the material's
510 Pb(II) removal efficiency in the presence of other co-existing heavy metals. Desorption with
511 EDTA makes the spent material fit for potential reuse over a greater number of cycles than an
512 acid treatment, but disposal of the Pb-EDTA might pose a secondary environmental issue
513 because of the strong binding strength in the metal-EDTA complex. This may potentially be
514 addressed by alkali (Kim and Ong, 1999) precipitation of the concerned solution, but further
515 research is necessary to better understand and address these issues.

516

517 **4. Conclusions**

518 Palygorskite-iron oxide nanocomposite was successfully synthesized by a co-precipitation
519 method and applied as an adsorbent of aqueous Pb(II). Pal-IO exhibited a high specific
520 surface area (99.8 $m^2 g^{-1}$), low isoelectric point (3.5) and significant magnetic susceptibility
521 (20.2 emu g^{-1}) that facilitated its potential application as an adsorbent for removing Pb(II).
522 The maximum Pb(II) adsorption capacity of 26.6 mg g^{-1} at pH 5 was achieved for the

treatment of contaminated water containing up to 200 mg L^{-1} Pb(II). EDTA-Na_2 was the best desorbing agent for regenerating the magnetic adsorbent with more than 90% desorption capability. Three consecutive adsorption-desorption cycles yielded more than 64% removal of Pb(II) at the end. The strong binding of iron oxide nanoparticles on palygorskite, the nanocomposite's superior magnetic properties and the least leaching of iron verified the magnetic stability and recyclability of Pal-IO. The nanocomposite could emerge as a promising material for purifying wastewaters contaminated especially with heavy metal cations.

Acknowledgments

This study was partially supported by the Clay Minerals Society (CMS) Student Research Grant (2016). Ruhaida Rusmin acknowledges the Ministry of Higher Education of Malaysia and Universiti Teknologi MARA for the PhD scholarship award. The authors acknowledge Dr Xiang Zhao from the Earth Environment Paleomagnetism Laboratory, Australian National University, for assistance with the VSM measurement, and Mr. Stuart McClure (University of South Australia) for the SEM analysis.

References

Ambashta, R.D., Sillanpää, M., 2010. Water purification using magnetic assistance: A review. Journal of Hazardous Materials 180, 38-49.

ATSDR, 2015. Agency for Toxic Substances and Disease Registry (ATSDR), Substance Priority List 2015. U.S. Department of Health and Human Services, USA.

Baumgartner, J., Dey, A., Bomans, P.H.H., Le Coadou, C., Fratzl, P., Sommerdijk, N.A.J.M., Faivre, D., 2013. Nucleation and growth of magnetite from solution. Nature Materials 12, 310-314.

548 Brigante, M., Pecini, E., Avena, M., 2016. Magnetic mesoporous silica for water remediation:
549 Synthesis, characterization and application as adsorbent of molecules and ions of
550 environmental concern. Microporous and Mesoporous Materials 230, 1-10.
551 Chen, J., Yan, L.-g., Yu, H.-q., Li, S., Qin, L.-l., Liu, G.-q., Li, Y.-f., Du, B., 2016b. Efficient
552 removal of phosphate by facile prepared magnetic diatomite and illite clay from
553 aqueous solution. Chemical Engineering Journal 287, 162-172.
554 Chen, L., Zhou, C.H., Fiore, S., Tong, D.S., Zhang, H., Li, C.S., Ji, S.F., Yu, W.H., 2016a.
555 Functional magnetic nanoparticle/clay mineral nanocomposites: preparation,
556 magnetism and versatile applications. Applied Clay Science 127–128, 143-163.
557 Cheng, H., Yang, J., Frost, R.L., 2011. Thermogravimetric analysis-mass spectrometry (TG-
558 MS) of selected Chinese palygorskites—Implications for structural water.
559 Thermochimica Acta 512, 202-207.
560 El-Bayaa, A.A., Badawy, N.A., AlKhalik, E.A., 2009. Effect of ionic strength on the
561 adsorption of copper and chromium ions by vermiculite pure clay mineral. Journal of
562 Hazardous Materials 170, 1204-1209.
563 Frost, R.L., Ding, Z., 2003. Controlled rate thermal analysis and differential scanning
564 calorimetry of sepiolites and palygorskites. Thermochimica Acta 397, 119-128.
565 Giles, C.H., MacEwan, T.H., Nakhwa, S.N., Smith, D., 1960. Studies in adsorption. Part XI.
566 A system of classification of solution adsorption isotherms, and its use in diagnosis of
567 adsorption mechanisms and in measurement of specific surface areas of solids.
568 Journal of the Chemical Society (Resumed), 3973-3993.
569 Guggenheim, S., Groos, A.F.K.V., 2001. Baseline studies of the Clay Minerals Society
570 source clays: thermal analysis. Clays and Clay Minerals 49.
571 Gunasekaran, S., Anbalagan, G., Pandi, S., 2006. Raman and infrared spectra of carbonates
572 of calcite structure. Journal of Raman Spectroscopy 37, 892-899.

573 Han, Y., Cao, X., Ouyang, X., Sohi, S.P., Chen, J., 2016. Adsorption kinetics of magnetic
574 biochar derived from peanut hull on removal of Cr (VI) from aqueous solution:
575 Effects of production conditions and particle size. Chemosphere 145, 336-341.
576 Harvey, P.J., Handley, H.K., Taylor, M.P., 2015. Identification of the sources of metal (lead)
577 contamination in drinking waters in north-eastern Tasmania using lead isotopic
578 compositions. Environmental Science and Pollution Research 22, 12276-12288.
579 Ho, Y.S., McKay, G., 1999. Pseudo-second order model for sorption processes. Process
580 Biochemistry 34, 451-465.
581 Huang, M.-R., Lu, H.-J., Li, X.-G., 2007. Efficient multicyclic sorption and desorption of
582 lead ions on facilely prepared poly(m-phenylenediamine) particles with extremely
583 strong chemoresistance. Journal of Colloid and Interface Science 313, 72-79.
584 Illés, E., Tombácz, E., 2006. The effect of humic acid adsorption on pH-dependent surface
585 charging and aggregation of magnetite nanoparticles. Journal of Colloid and Interface
586 Science 295, 115-123.
587 Issa, B., Obaidat, I.M., Albiss, B.A., Haik, Y., 2013. Magnetic Nanoparticles: Surface Effects
588 and Properties Related to Biomedicine Applications. International Journal of
589 Molecular Sciences 14, 21266-21305.
590 Kim, C., Ong, S.-K., 1999. Recycling of lead-contaminated EDTA wastewater. Journal of
591 Hazardous Materials 69, 273-286.
592 Kim, K.-J., Kim, D.-H., Yoo, J.-C., Baek, K., 2011. Electrokinetic extraction of heavy metals
593 from dredged marine sediment. Separation and Purification Technology 79, 164-169.
594 Kumari, M., Pittman, C.U., Mohan, D., 2015. Heavy metals [chromium (VI) and lead (II)]
595 removal from water using mesoporous magnetite (Fe_3O_4) nanospheres. Journal of
596 Colloid and Interface Science 442, 120–132.

Lee, P.-L., Chiu, Y.-K., Sun, Y.-C., Ling, Y.-C., 2010. Synthesis of a hybrid material consisting of magnetic iron-oxide nanoparticles and carbon nanotubes as a gas adsorbent. Carbon 48, 1397-1404.

Lottermoser, B. G., 2010. Mine Water. In: Lottermoser, B. G. (3rd Ed.). Mine Wastes. Springer Berlin Heidelberg, pp. 119–203.

Liu, H., Chen, W., Liu, C., Liu, Y., Dong, C., 2014. Magnetic mesoporous clay adsorbent: Preparation, characterization and adsorption capacity for atrazine. Microporous and Mesoporous Materials 194, 72-78.

Ma, Z., Guan, Y., Liu, H., 2005. Synthesis and characterization of micron-sized monodisperse superparamagnetic polymer particles with amino groups. Journal of Polymer Science Part A: Polymer Chemistry 43, 3433-3439.

Madejová, J., Komadel, P., 2001. Baseline studies of the clay minerals society source clays: infrared methods. Clays and Clay Minerals 49, 410-432.

Mahdavian, A.R., Mirrahimi, M.A.-S., 2010. Efficient separation of heavy metal cations by anchoring polyacrylic acid on superparamagnetic magnetite nanoparticles through surface modification. Chemical Engineering Journal 159, 264-271.

Mandel, K., Hutter, F., Gellermann, C., Sextl, G., 2011. Synthesis and stabilisation of superparamagnetic iron oxide nanoparticle dispersions. Colloids and Surfaces A: Physicochemical and Engineering Aspects 390, 173-178.

Murray, H.H., 2006. Chapter 2 Structure and Composition of the Clay Minerals and their Physical and Chemical Properties. in: Haydn, H.M. (Ed.). Developments in Clay Science. Elsevier, pp. 7-31.

Naidu, R., 2013. Recent advances in contaminated site remediation. Water, Air, & Soil Pollution 224, 1705.

621 Namduri, H., Nasrazadani, S., 2008. Quantitative analysis of iron oxides using Fourier
622 transform infrared spectrophotometry. Corrosion Science 50, 2493-2497.
623 Norén, K., Loring, J.S., Bargar, J.R., Persson, P., 2009. Adsorption mechanisms of EDTA at
624 the water−iron oxide interface: implications for dissolution. The Journal of Physical
625 Chemistry C 113, 7762-7771.
626 Pan, J., Xu, L., Dai, J., Li, X., Hang, H., Huo, P., Li, C., Yan, Y., 2011. Magnetic molecularly
627 imprinted polymers based on attapulgite/Fe3O4 particles for the selective recognition
628 of 2,4-dichlorophenol. Chemical Engineering Journal 174, 68-75.
629 Sarkar, B., Liu, E., McClure, S., Sundaramurthy, J., Srinivasan, M., Naidu, R., 2015.
630 Biomass derived palygorskite–carbon nanocomposites: Synthesis, characterisation
631 and affinity to dye compounds. Applied Clay Science 114, 617-626.
632 Sarkar, B., Xi, Y.F., Megharaj, M., Krishnamurti, G.S.R., Bowman, M., Rose, H., Naidu, R.,
633 2012. Bioreactive organoclay: a new technology for environmental remediation.
634 Critical Reviews in Environmental Science and Technology 42, 435-488.
635 Shahbazi, A., Younesi, H., Badiei, A., 2013. Batch and fixed-bed column adsorption of
636 Cu(II), Pb(II) and Cd(II) from aqueous solution onto functionalised SBA-15
637 mesoporous silica. The Canadian Journal of Chemical Engineering 91, 739-750.
638 Su, C., 2017. Environmental implications and applications of engineered nanoscale magnetite
639 and its hybrid nanocomposites: A review of recent literature. Journal of Hazardous
640 Materials 322, Part A, 48-84.
641 Suárez, M., García-Romero, E., 2006. FTIR spectroscopic study of palygorskite: Influence of
642 the composition of the octahedral sheet. Applied Clay Science 31, 154-163.
643 Tian, X., Wang, W., Tian, N., Zhou, C., Yang, C., Komarneni, S., 2016. Cr(VI) reduction and
644 immobilization by novel carbonaceous modified magnetic Fe3O4/halloysite
645 nanohybrid. Journal of Hazardous Materials 309, 151-156.

646 Tombácz, E., Csanaky, C., Illés, E., 2001. Polydisperse fractal aggregate formation in clay
647 mineral and iron oxide suspensions, pH and ionic strength dependence. Colloid and
648 Polymer Science 279, 484-492.
649 Tombácz, E., Turcu, R., Socoliuc, V., Vékás, L., 2015. Magnetic iron oxide nanoparticles:
650 Recent trends in design and synthesis of magnetoresponsive nanosystems.
651 Biochemical and Biophysical Research Communications 468(3), 442–453.
652 Tsuzuki, T., Schäffel, F., Muroi, M., McCormick, P.G., 2011. Magnetic properties of
653 mechanochemically synthesized γ-Fe2O3 nanoparticles. Journal of Alloys and
654 Compounds 509, 5420-5425.
655 Udovic, M., Lestan, D., 2012. EDTA and HCl leaching of calcareous and acidic soils
656 polluted with potentially toxic metals: Remediation efficiency and soil impact.
657 Chemosphere 88, 718-724.
658 Xiang, B., Fan, W., Yi, X., Wang, Z., Gao, F., Li, Y., Gu, H., 2016. Dithiocarbamate-
659 modified starch derivatives with high heavy metal adsorption performance.
660 Carbohydrate Polymers 136, 30-37.
661 Xu, P., Zeng, G.M., Huang, D.L., Feng, C.L., Hu, S., Zhao, M.H., Lai, C., Wei, Z., Huang,
662 C., Xie, G.X., Liu, Z.F., 2012. Use of iron oxide nanomaterials in wastewater
663 treatment: A review. Science of The Total Environment 424, 1-10.
664 Yoshida, A., Terazono, A., Ballesteros Jr, F.C., Nguyen, D.-Q., Sukandar, S., Kojima, M.,
665 Sakata, S., 2016. E-waste recycling processes in Indonesia, the Philippines, and
666 Vietnam: A case study of cathode ray tube TVs and monitors. Resources,
667 Conservation and Recycling 106, 48-58.
668

Highlights

- Superparamagnetic palygorskite nanocomposite was synthesized and characterized
- The nanocomposite adsorbed up to 63% more Pb^{2+} than palygorskite
- Easy magnetic separation of spent adsorbent was achieved within 60 to 120 sec
- EDTA performed the best to regenerate the spent adsorbent
- Magnetic susceptibility after 3 cycles of use reduced only slightly